Subject-Specific Modeling of EEG-fNIRS Neurovascular Coupling by Task-Related Tensor Decomposition

Jianeng Lin, Jiewei Lu, Zhilin Shu, Jianda Han, *Member, IEEE*, and Ningbo Yu, *Member, IEEE*

***Abstract*— Neurovascular coupling (NVC) connects neural activity with hemodynamics and plays a vital role in sustaining brain function. Combining electroencephalography (EEG) and functional near-infrared spectroscopy (fNIRS) is a promising way to explore the NVC. However, the high-order property of EEG data and variability of hemodynamic response function (HRF) across subjects have not been well considered in existing NVC studies. In this study, we proposed a novel framework to enhance the subject-specific parametric modeling of NVC from simultaneous EEG-fNIRS measurement. Specifically, task-related tensor decomposition of high-order EEG data was performed to extract the underlying connections in the temporal-spectral-spatial structures of EEG activities and identify the most relevant temporal signature within multiple trials. Subject-specific HRFs were estimated by parameters optimization of a double gamma function model. A canonical motor task experiment was designed to induce neural activity and validate the effectiveness of the proposed framework. The results indicated that the proposed framework significantly improves the reproducibility of EEG components and the correlation between the predicted hemodynamic activities and the real fNIRS signal. Moreover, the estimated parameters characterized the NVC differences in the task with two speeds. Therefore, the proposed framework provides a feasible solution for the quantitative assessment of the NVC function.**

***Index Terms*— Neurovascular coupling, EEG-fNIRS, tensor decomposition, task-related component analysis, hemodynamic response function, subject-specific optimization.**

Manuscript received 17 July 2023; revised 3 January 2024; accepted 12 January 2024. Date of publication 17 January 2024; date of current version 24 January 2024. This work was supported in part by the National Key Research and Development Program of China under Grant 2022YFB4700203, in part by the National Natural Science Foundation of China under Grant U1913208, in part by the Science and Technology Program of Tianjin under Grant 21JCZDJC00170, and in part by the Excellent Youth Team of Central Universities under Grant NKU-63231196. *(Corresponding authors: Jianda Han; Ningbo Yu.)*

This work involved human subjects or animals in its research. Approval of all ethical and experimental procedures and protocols was granted by the Ethics Committees of Nankai University.

Jianeng Lin, Jiewei Lu, and Zhilin Shu are with the College of Artificial Intelligence, Nankai University, Tianjin 300350, China.

Jianda Han and Ningbo Yu are with the College of Artificial Intelligence, Nankai University, Tianjin 300350, China, and also with the Institute of Intelligence Technology and Robotic Systems, Shenzhen Research Institute of Nankai University, Shenzhen 518083, China (e-mail: hanjianda@nankai.edu.cn; nyu@nankai.edu.cn).

Digital Object Identifier 10.1109/TNSRE.2024.3355121

I. Introduction

NEUROVASCULAR coupling (NVC) refers to the close functional relationship between neuronal activity and hemodynamic-related changes in the brain [1]. It maintains adequate blood flow and oxygen supply to the active brain regions during neuronal activity [2]. NVC plays a critical role in various physiological processes, including motor and cognitive functions [3], [4], [5]. The disruptions of NVC could lead to impaired brain functions and have been associated with various neurological disorders such as stroke and Alzheimer's disease [6], [7]. Therefore, understanding the mechanisms underlying NVC is crucial for improving our understanding of brain functions and developing effective diagnostic and therapeutic methods for neurological disorders.

The simultaneous measurement of electrophysiological and hemodynamic activities, such as combining electroencephalography (EEG) with functional magnetic resonance imaging (fMRI), can be used to study NVC [8]. The canonical approach to quantify NVC in EEG-fMRI studies is to compare the blood oxygen level dependent (BOLD) time course with the convolution of the canonical hemodynamic function (HRF) and EEG feature [9], [10]. The general linear model (GLM) was used as a standard method to estimate the coupling strength and identify brain regions showing significant coupling. GLM offers enhanced capabilities in detecting temporal dynamics and making statistical inference than other methods like correlation analysis. The alpha rhythm of EEG was found to be negatively correlated with the BOLD signal of fMRI in both resting and task states [11], [12].

For the past few years, the combination of EEG with another non-invasive hemodynamic neuroimaging technique, functional near-infrared spectroscopy (fNIRS), has become an attractive technique to investigate NVC. fNIRS measures the relative change in hemoglobin concentration to infer neural activity [13]. Compared to EEG-fMRI, EEG-fNIRS is more flexible, less costly, and free of electromagnetic interference [10]. Some studies have been trying to explore NVC by EEG-fNIRS. Similar to EEG-fMRI, the methods based on HRF and GLM remain the mainstream approaches for NVC analysis [3], [14], [15]. However, such approaches still have limitations in the following aspects. First, most studies set quite strict constraints in EEG feature extraction, such

as selecting a portion of interested electrodes and spectral bands and averaging the results. The predefined selection is subjective and strongly dependent on prior knowledge. Moreover, such approaches ignore the couplings within and between different channels or spectral bands, which could be the key to NVC analysis. Second, most studies used the canonical HRF for dealing with the time delay nature of hemodynamic signals in NVC quantification [16]. However, the HRF is known to vary across individuals and brain regions due to differences in vascular density, metabolic demand, and vascular tone [17]. The fixed shape and parameters of the canonical HRF imply several assumptions and could not reflect the subject-specific NVC. Moreover, most NVC studies assumed that their analysis methods are effective and lacked a systematic comparison of the differences in analysis results caused by different EEG features and transfer functions.

To this end, we proposed a novel framework to enhance the subject-specific parametric modeling of NVC from simultaneous EEG-fNIRS measurement. Specifically, task-related tensor decomposition of high-order EEG data was performed to extract the underlying connections in the structures of EEG activities and identify the most relevant temporal signature within multiple trials. Subject-specific HRFs were estimated by parameters optimization of a double gamma function model. A systematical comparison of different EEG features and HRFs with quantitative indicators and cross-validation was performed. The effectiveness of the proposed framework was verified on the data with 16 healthy participants during the typical motor tasks. We expected the proposed framework could provide a feasible way to enhance NVC analysis compared to the canonical methods.

II. Materials and Methods

A. Participants

A prior statistical power analysis was performed using GPower 3.1.9.4 software to estimate the minimum sample size required for the statistical test [18]. The significance level (α) and the power ($1-\beta$) were set as 0.05 and 0.8 [19]. Since similar previous studies showed tensor decomposition could significantly enhance the EEG-fMRI analysis, we anticipated a large effect size of 0.8 using Cohen's criteria [20], [21], [22]. Results of the power analysis show that the sample size needed with this effect size is approximately N = 15 to detect significant effects. Sixteen young adults (age: 24.5 ± 1.9 years, all males) took part in this experiment. None of the recruited participants had any neurological diseases or movement impairments. They were right-handedness confirmed by the Edinburgh Handedness Inventory. Each participant signed the informed consent before the formal experiment. This study was approved by the Ethics Committee of Nankai University.

B. Experimental Protocol

The experiment included two sessions, each corresponding to one task speed. Each session consisted of 15 trials, and each trial comprised a 10-second task period along with a subsequent 20-second rest period, as shown in Fig. 1(a). During the task period, participants were instructed to tap their right index finger following a metronome at 1 or 2 Hz, as shown in Fig. 1(b). During the rest period, participants were instructed to look at the center of the screen and keep their whole body relaxed and reduce movement. The experimental protocol was realized by a custom program developed by E-prime 3.0 (Psychology Software Tools, PA, USA).

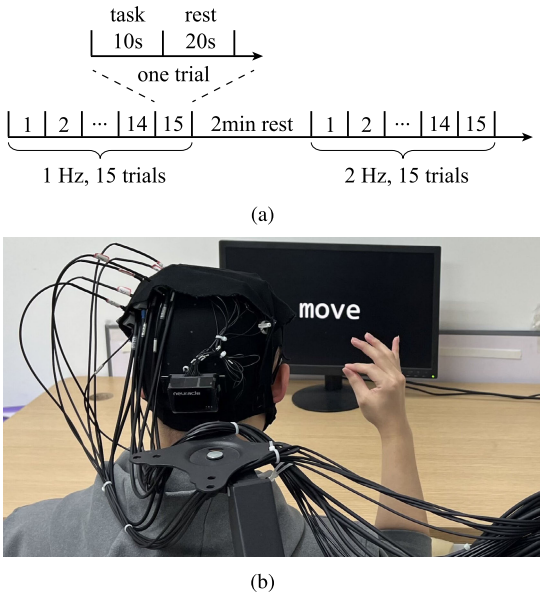

Fig. 1. The experimental procedures. (a) Experimental paradigm for the finger tapping tasks. (b) Participants performed the finger tapping tasks with 1 Hz and 2 Hz frequencies following the instructions from the screen and metronome.

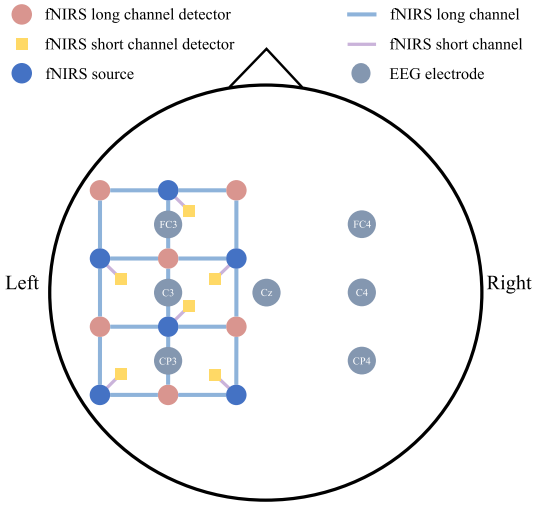

Fig. 2. The channel arrangement of EEG-fNIRS measurement. Eighteen fNIRS probes (six sources, six long channel detectors, and six short channel detectors) were placed at the left motor cortex, resulting in 17 long-distance (3 cm) and six short-distance (1 cm) channels. Seven electrodes were placed at the bilateral motor cortex.

C. Data Acquisition

The EEG-fNIRS signals were recorded simultaneously by a customized acquisition cap, as shown in Fig. 2. The synchronization of EEG and fNIRS signals was realized by sending markers to a trigger box. The scalp EEG signals were recorded

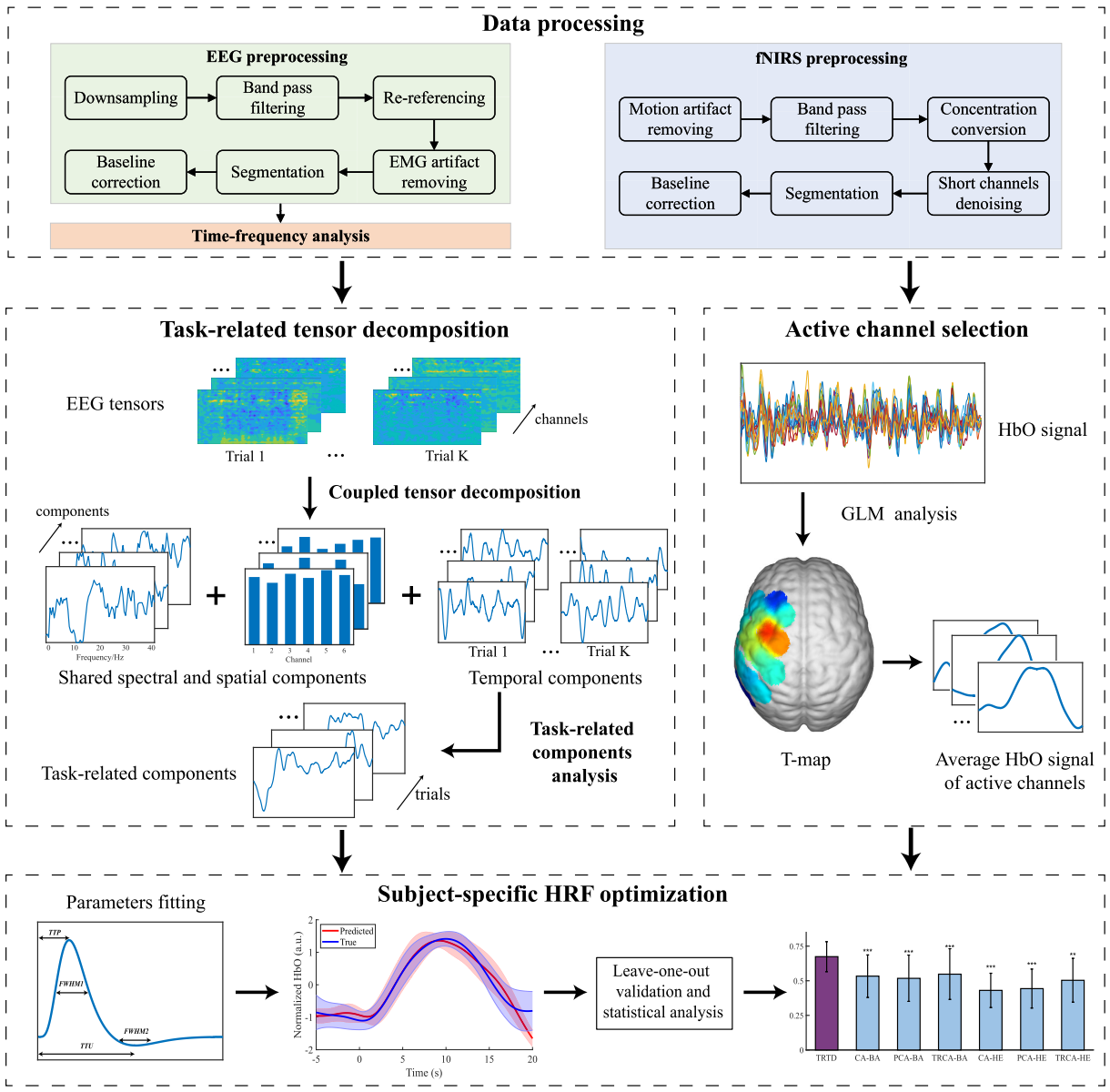

Fig. 3. Schematic diagram of the complete analysis framework. The bimodal EEG-fNIRS signals were pre-processed first. For EEG data, time-frequency analysis was performed on EEG data to convert it to tensor format. Shared spectral and spatial components were extracted by coupled tensor decomposition. The task-related components were obtained from the corresponding temporal components within multiple trials. For fNIRS data, active channels were identified by GLM. Then, the task-related EEG temporal components were used to fit the averaged active HbO signal. Subject-specific HRFs were estimated by parameters optimization of a double gamma function model. Finally, the leave-one-out validation and statistical analysis were conducted to validate the effectiveness of the proposed framework.

with the NeusenW system (Neuracle Inc, China) at 1000 Hz. Seven EEG electrodes (FC3, C3, CP3, Cz, FC4, C4, CP4) distributed in the motor cortex were selected and integrated into the bimodal acquisition cap according to the international 10-20 system. The impedance of each electrode was ensured to be reduced below 10 kΩ before the data recording. The fNIRS signals were recorded by the Nirsmart system (Danyang Huichuang, China) at 30 Hz. The wavelengths of near-infrared light were 760 nm and 850 nm. A total of six sources and six detectors constituted 17 fNIRS long channels, covering the sensorimotor cortex (SMC) and the premotor cortex (PMC). The inter-optode distance of long channels was 3 cm. In addition, six detectors were placed 1 cm away from the sources, forming six fNIRS short channels to measure the physiological noise.

D. Proposed Method

1) Data Preprocessing: The schematic diagram of the complete analysis framework is shown in Fig. 3. EEG preprocessing was performed using a MATLAB toolbox, EEGLAB (Swartz Center for Computational Neuroscience, USA) [23]. The EEG data were first downsampled to 250 Hz and filtered from 1-40 Hz. Muscle artifacts were reduced by the BSS-CCA method [24]. Then, the EEG data were segmented into 20-second epochs (−5 to 15 s) and baseline corrected.

Time-frequency analysis of EEG data was performed using the short-time Fourier transform (STFT) with a 0.5 Hz frequency resolution. The number of time windows of the 20-second data was set to 600, i.e., the temporal resolution was 30 Hz and was equal to the sampling rate of the fNIRS

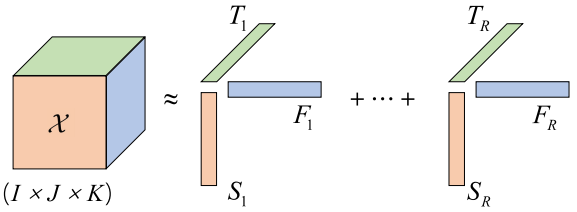

Fig. 4. Illustration of the CPD of the three-dimensional EEG tensor.

signal. Finally, the baseline level of 5 seconds is subtracted from the calculated result.

The fNIRS signals were preprocessed using the HOMER 3 implemented in MATLAB [25]. First, wavelet filtering was used to remove the motion artifacts of fNIRS data [26]. The parameter iqr was set to the default value (1.5) to detect outliers [27]. Then, a Butterworth bandpass filter at 0.01-0.2 Hz was utilized to remove the physiological noises (e.g., heartbeat and respiration) of fNIRS data. Next, the modified Beer–Lambert law was employed to convert the fNIRS data into the relative concentration changes of oxy-hemoglobin (HbO). The physiological noises measured by the short fNIRS channels were utilized to create the additional noise regressors, which were subsequently regressed out from fNIRS data using the GLM [28]. Finally, the data epochs were extracted and baseline corrected, consistent with EEG preprocessing.

2) Tensor Decomposition of EEG Data: EEG signals are multi-way in nature. For instance, there may be modes such as group, subject, trial, time, frequency, and channel in EEG experiments [29]. Tensor decomposition allows for the simultaneous analysis of multiple dimensions of EEG data, enabling a more comprehensive understanding of brain activities [30]. To process EEG data by tensor decomposition, it is first necessary to perform time-frequency analysis to convert it into tensor form. In this case, a three-dimensional tensor $\mathcal{X} \in \mathbb{R}^{I \times J \times K}$ is commonly used, with one mode representing time, another representing frequency, and the last one representing channel, and I, J, and K are their dimensions for each mode, respectively. Then, the two primary models could be used for tensor decomposition of EEG data, including canonical polyadic decomposition (CPD) and Tucker decomposition (TD) [29]. We chose CPD for further analysis since it has advantages in the simplicity of component number selection and the uniqueness of solution compared to TD [30]. Generally, the CPD of the three-dimensional tensor $\mathcal{X}^{I \times J \times K}$ is defined as:

$$\mathcal{X} = \sum_{r=1}^{R} S_r \circ F_r \circ T_r \tag{1}$$

where R indicates the number of components, S, F, and T indicate the rank-1 spatial, frequency, and time tensors, respectively. An illustration of the CPD of the three-dimensional EEG tensor can be seen in Fig. 4.

3) Task-Related Tensor Decomposition (TRTD) of EEG Data: Due to the low signal-to-noise ratio (SNR) of EEG data, multiple trials of the same task are needed to be repeated in an EEG experiment typically. It forms another important dimension of EEG tensor, i.e., trials. Analyzing a 4-dimensional tensor assumed that the spatial, temporal, and spectral information were consistent among all the trials [31]. This assumption is difficult to satisfy due to the high variability of EEG data. Therefore, we proposed the task-related tensor decomposition (TRTD) to extract the sharing task-related information within multiple trials of tensors.

The TRTD framework was informed by prior studies using coupled tensor decomposition for EEG data analysis [31], [32]. These studies hypothesized that the spectral and spatial components are shared among different subjects. In our study, the TRTD was performed within the subjects. In the first step, we assumed that the spatial and spectral components are shared among K trials, while there is variability in the time-domain components. This is a more relaxed assumption since the individual difference was excluded. In addition, nonnegative constraints were imposed on spatial and spectral components to obtain meaningful solutions. The optimization objective was obtained as follows:

$$\begin{aligned} &\min \sum_{k=1}^{K} \left\| \mathcal{X}^{(k)} - \sum_{r=1}^{R} S_r \circ F_r \circ T_r^{(k)} \right\|_F^2 \\ &s.t.\ S_r >= 0, F_r >= 0 \end{aligned} \tag{2}$$

where k denotes the trial index, r denotes the component index, R denotes the number of components, S, F, and T denote the spatial, frequency, and time components, respectively. The number of components R was set to six, which was equal to the number of available channels (Cz was used as the reference). The solving of tensor decomposition was using the Tensorlab 3.0 implemented in MATLAB [33].

Considering that the data was recorded under the same task and with the same participant, it was logical to anticipate a high correlation between the temporal information evoked by the task across multiple trials. Meanwhile, since the spatial and spectral components were identical within multiple trials, the order of components in each trial was fixed, which was the prerequisite for applying task-related component analysis (TRCA). To this end, in the second step, the $1*R$-dimensional component filter $\mathbf{w}$ was solved by TRCA, and the components were weighted and summed to extract the most correlated components among the K trials [34]:

$$\begin{aligned} \hat{\mathbf{w}} &= \arg\max_{\mathbf{w}} \frac{\mathbf{w}^{\mathrm{T}}\mathbf{S}\mathbf{w}}{\mathbf{w}^{\mathrm{T}}\mathbf{Q}\mathbf{w}} \\ \mathbf{S}_{ij} &= \sum_{\substack{k,l=1 \\ k \neq l}}^{K} \mathrm{Cov}\left(X_i^{(k)}, X_j^{(l)}\right) \\ \mathbf{Q} &= \sum_{i,j=1}^{R} \mathrm{Cov}\left(X_i, X_j\right) \end{aligned} \tag{3}$$

where X represents the temporal components, R represents the number of components, K represents the number of trials, i and j represent the indexes of components, k and l represent the indexes of trials. The solution of optimization problem could be obtained as R eigenvectors of the matrix $Q^{-1}S$ [34].

4) Active Channel Selection of fNIRS Data: In this study, the GLM was utilized to estimate the level of activation for each

fNIRS channel.

$$Y = G\boldsymbol{\beta} + E \tag{4}$$

where Y is the fNIRS signal, $\boldsymbol{\beta}$ is the channel weights, E is the error matrix, and G is the design matrix, including the regressors of a constant and the convolution of the canonical HRF with the stimulus function. The estimate of weights $\widehat{\boldsymbol{\beta}}$ were obtained by robust regression, which was achieved by the $robustfit$ function in Matlab. T-test was conducted to identify the channels that rejected the null hypothesis $\boldsymbol{\beta} = 0$ ($p < 0.05$) significantly:

$$\mathrm{t} = \frac{c^T\widehat{\boldsymbol{\beta}}}{\sqrt{\widehat{\sigma}^2 c^T \left(G^T G\right)^{-1} c}} \tag{5}$$

where c is the channel selection vector, $\widehat{\sigma}^2$ is the residual sum-of-squares divided by the degrees of freedom. Three channels with the highest activation levels (i.e., t values) were selected and averaged for further analysis.

5) Subject-Specific Neurovascular Coupling Modeling: Due to the variability of HRF, we aim to build a within-subject model with subject-specific parameters to enhance the analysis. The model structure is general to all the subjects, but the model parameters are subject-specific and could be obtained by subject-specific optimization. The two-gamma functions model was chosen for parameterizing the HRF due to its physiological accuracy in representing the HRF and widespread acceptance in both fMRI and fNIRS research [35]:

$$HRF(t) = \frac{b_1^{a_1} t^{(a_1-1)}}{\Gamma(a_1)} e^{(-b_1 t)} - \frac{b_2^{a_2} t^{(a_2-1)}}{c\Gamma(a_2)} e^{(-b_2 t)} \tag{6}$$

where t represents the time points, b_1 and b_2 represent the dispersion time constants for the peak and undershoot periods, a_1 and a_2 represent the peak time and undershoot time, c represents the ratio of the amplitude of the peak to the undershoot, and Γ represents the gamma function. The parameters of canonical HRF were set as ($b_1, b_2 = 1$, $a_1 = 6, a_2 = 16$, $c = 6$) in NIRS-SPM toolbox [36].

Shape parameters including the time to peak (TTP), the time to undershoot (TTU), and the full width at half maximum of the first and the second gamma function ($FWHM1$, $FWHM2$) could be calculated as [35]:

$$\begin{aligned} TTP &= a_1/b_1 \\ TTU &= a_2/b_2 \\ FWHM1 &= 2.35\sqrt{a_1 - 1}/b_1 \\ FWHM2 &= 2.35\sqrt{a_2 - 1}/b_2 \end{aligned} \tag{7}$$

An illustration of these parameters is shown in Fig. 5. We proposed constraints on both the argument of the function and the shape parameters: $a_1 \in [2, 10]$, $a_2 \in [6, 25]$, $b_1 \in [0.5, 2]$, $b_2 \in [0, 1.5]$, $c \in [0, 15]$; $TTP \in [3, 7]$, $TTU \in [9, 18]$, $FWHM1 \in [3, 6]$, and $FWHM2 \in [7, 11]$ [35].

In total, the optimization function was proposed as follows:

$$\min_{a_1,a_2,b_1,b_2,c} \sum_{k=1}^{K}\sum_{t=1}^{T} \left({y_{HbO}}^{(k)}(t) - HRF(t) \otimes T_{EEG}(t) \right)^2 \tag{8}$$

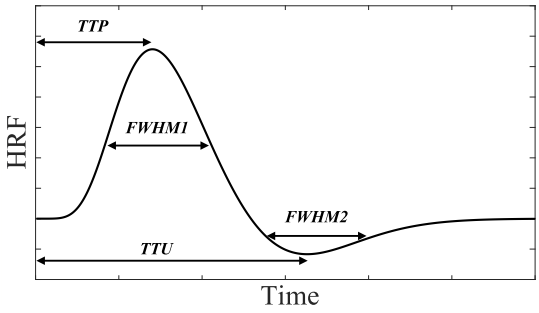

Fig. 5. Illustration of the parameters of the canonical HRF. TTP/TTU and FWHM1/2 are the time to peak/undershoot and the full width at half maximum of the positive phase of the HRF for the first/second gamma function, respectively.

where K and k indicate the total number and index of trials. y_{HbO} indicates the real HbO signal. T_{EEG} indicates the task-related temporal components decomposed from EEG data, and t indicates the time index. The optimization was realized by the interior point method using the optimization toolbox in MATLAB, and the initial points were chosen as the values of parameters in the canonical HRF.

E. Performance Evaluation

1) EEG Decomposition: First, we evaluated the reproducibility of the extracted temporal components using the inter-trial similarity (ITS):

$$\begin{aligned} P &= \frac{1}{K}\sum_{k=1}^{K} Y^{(k)} \\ ITS &= \frac{1}{K}\sum_{k=1}^{K} \mathrm{corr}\left(Y^{(k)}, P\right) \end{aligned} \tag{9}$$

where K and k indicate the total number and index of trials.

Second, we computed the mean correlation between the extracted temporal components and the stimulus function ($Corr_{sti}$) [21]:

$$Corr_{sti} = \frac{1}{K}\sum_{k=1}^{K} \mathrm{corr}\left(Y^{(k)}, Stimulus\right) \tag{10}$$

2) Neurovascular Coupling Modeling: For each participant, we computed the Pearson's correlation coefficients (PCC) and normalized root mean square error (NRMSE) between the fitted fNIRS signal and the actual fNIRS signal. The modeling performance was evaluated using leave-one-out cross-validation. In each iteration of validation, the test data consisted of one trial while the training data comprised the remaining data from other trials. The sharing spatial and spectral components and the components filter were obtained after performing TRTD with the training data. The test data was then decomposed by constrained tensor decomposition, i.e., the spatial and spectral components were constant and the same as the training data. After decomposition, the temporal components were filtered by the components filter obtained from the training data.

3) Compared Methods: Three typical spatial filtering methods were chosen for comparison, including channel-averaged (CA), principle component analysis (PCA), and task-related component analysis (TRCA). Two spectral filtering methods were chosen for comparison, including band-averaged (BA) and Heuristic model (HE). Specifically, for BA, the time-frequency data of the five canonical bands, including the delta (1-3 Hz), theta (3-8 Hz), alpha (8-13 Hz), beta (13-30 Hz), and low gamma (30-40 Hz) bands were averaged for all frequency points of each band, respectively. For HE, the combination of each frequency point of the time-frequency data in one trial was calculated as [37]:

$$Y_{\mathrm{HE}}(t) = \sqrt{\sum_{f=1}^{n_f} f^2 Y(f,t)} \tag{11}$$

where f and n_f denote the frequency point and the total number of frequency points. Then, three spatial filtering methods and two spectral filtering methods were combined in pairs to form a total of six comparative methods. To keep the brevity of this paper, the results were only reported in the frequency band with the best performance for BA-related methods. The optimized subjective HRF (sHRF) was compared with the canonical HRF (cHRF) only for the proposed TRTD methods.

4) Statistical Analysis: Shapiro–Wilk tests were utilized to ensure the normality of the data. Paired t-tests were used to check whether the differences in the performance indicators between the proposed TRTD method and the other compared methods were significant ($p < 0.05$). Effect sizes (Cohen's d) were further calculated for avoiding interference from the sample size. The critical values of small, medium, and large effect sizes were defined as 0.2, 0.5, and 0.8, respectively [20].

III. Results

A. Tensor Decomposition of EEG Data

The group-averaged temporal, spectral, and spatial components after the TRTD of the EEG data in two FT tasks are shown in Fig. 6. The Pearson's correlation coefficient between the group-averaged components of the FT tasks with two speeds is 0.963, indicating a high degree of consistency. The temporal components were highly modulated with the experimental paradigm, decreasing at the beginning of the task and gradually returning to baseline levels at the end of the task. For spectral components, the weight of the alpha band, beta band, and gamma band were higher compared to the delta and theta bands. For spatial components, the weight of C3 located at the left primary motor cortex (M1) was the highest among all the electrodes.

The ITS and $Corr_{sti}$ of the temporal components decomposed by TRTD and compared methods in two FT tasks are shown in Fig. 7 and Table I. The ITS and $Corr_{sti}$ of TRTD in both two tasks were significantly higher than the compared methods, which demonstrated the high reproducibility and consistency with the experimental paradigm of the TRTD method.

In summary, the combined qualitative and quantitative outcomes substantiated the efficacy of the TRTD method in decomposing the EEG signals.

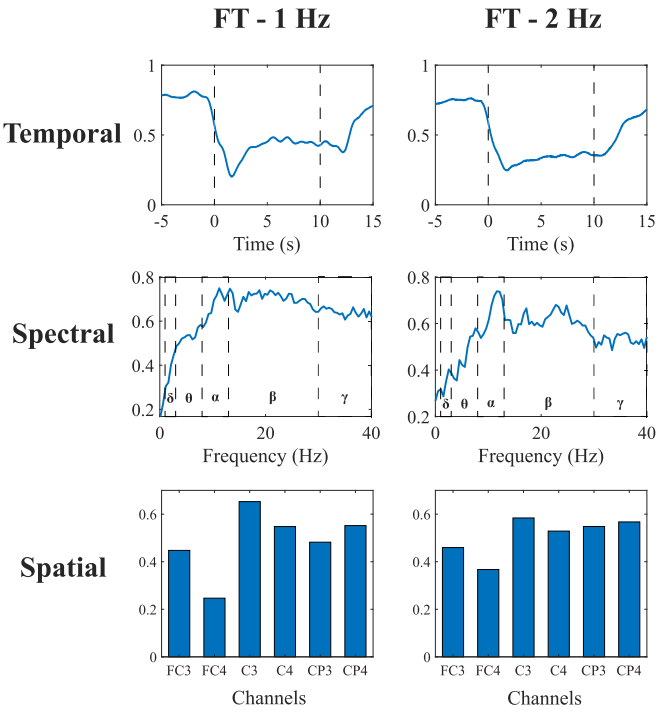

Fig. 6. Group-averaged temporal, spectral, and spatial components after the TRTD of the EEG data in two FT tasks. The vertical dashed lines in temporal components represent the beginning and end of the task. The vertical dashed lines in spectral components divide five frequency bands, including the delta, theta, alpha, beta, and low gamma frequency bands from left to right in sequence.

B. Active Channels Selection of fNIRS Data

Group-level activation maps for the two FT tasks estimated by GLM are shown in Fig. 8. The channel with the highest activation was located at the left primary motor cortex (M1) for both two tasks, and the highest activation level of the 2 Hz FT task (0.910) was higher than 1 Hz (0.836).

C. Subject-Specific Neurovascular Coupling Modeling

An example of the comparison of the true HbO signal and the predicted signal fitted by convolving the temporal components of EEG and cHRF and sHRF of a typical participant is shown in Fig. 9. The signal predicted by cHRF had a mismatch in the time lag and the lasting time with the true HbO signal, while this mismatch was well compensated by the optimization of the sHRF. The parameters of sHRF are as follows: $a_1 = 5.459, a_2 = 14.039, b_1 = 1.486, b_2 = 0.771, c = 1.391$. The difference in these parameters with cHRF indicated the shorter peak times of the two gamma functions and the lower undershoot.

The PCC and NRMSE between the true HbO signal and the predicted signal fitted by the convolution of the sHRF and the temporal components decomposed by TRTD and compared methods in two FT tasks are shown in Fig. 10 and Table II. The PCC and NRMSE of TRTD in both two tasks all showed significant improvement to the compared methods except for the NRMSE of the TRCA-BA method in 2 Hz FT.

The PCC and NRMSE between the true HbO signal and the predicted signal fitted by the convolution of the temporal components decomposed by TRTD with the cHRF and

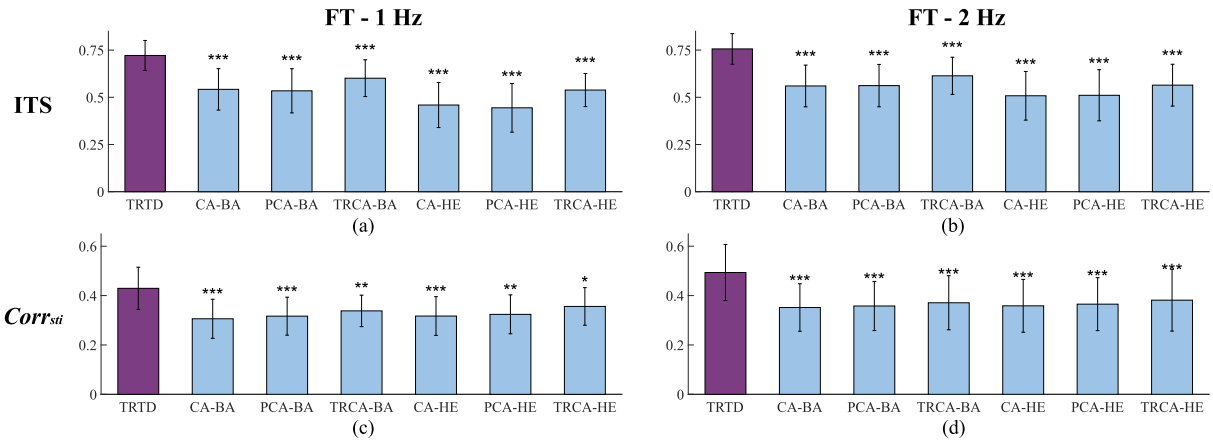

Fig. 7. The ITS and $Corr_{sti}$ of the temporal components decomposed by TRTD and compared methods in two FT tasks. Error bars represent standard deviation. The asterisks '*', '**', and '***' denote $p < 0.05$, $p < 0.01$, and $p < 0.001$, respectively.

TABLE I
THE ITS AND $Corr_{sti}$ OF THE TEMPORAL COMPONENTS DECOMPOSED BY THE TRTD AND COMPARED METHODS

Task	Metrics	Our TRTD method	CA-BA	PCA-BA	TRCA-BA	CA-HE	PCA-HE	TRCA-HE
FT - 1 Hz	ITS	**0.722±0.079**	0.542±0.109	0.534±0.117	0.601±0.097	0.459±0.119	0.444±0.129	0.538±0.088
	p-value		0.000***	0.000***	0.000***	0.000***	0.000***	0.000***
	Effect size		2.545	2.401	1.849	2.416	2.518	2.392
	Corr_sti	**0.429±0.086**	0.306±0.079	0.317±0.077	0.338±0.064	0.317±0.078	0.324±0.079	0.356±0.076
	p-value		0.000***	0.001***	0.003**	0.001***	0.002**	0.024*
	Effect size		1.193	1.077	0.874	1.026	0.943	0.626
FT - 2 Hz	ITS	**0.756±0.081**	0.560±0.111	0.562±0.112	0.614±0.099	0.508±0.129	0.511±0.135	0.564±0.111
	p-value		0.000***	0.000***	0.000***	0.000***	0.000***	0.000***
	Effect size		2.445	2.387	2.013	1.895	1.785	1.671
	Corr_sti	**0.493±0.114**	0.352±0.096	0.358±0.100	0.371±0.110	0.359±0.107	0.365±0.107	0.381±0.125
	p-value		0.000***	0.000***	0.000***	0.000***	0.000***	0.000***
	Effect size		2.208	2.087	1.551	1.876	1.790	1.219

The asterisks '*', '**', and '***' denote $p < 0.05$, $p < 0.01$, and $p < 0.001$, respectively.

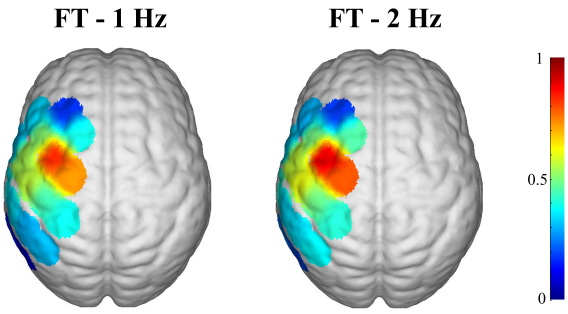

Fig. 8. Group-level activation maps for the two FT tasks estimated by GLM.

sHRF in two FT tasks are shown in Fig. 11. The PCC and NRMSE of TRTD in both two tasks were significantly improved (increased in PCC and decreased in NRMSE) than the compared methods. Specifically, the PCC in 1 Hz FT task (0.710) and 2 Hz FT task (0.725) using sHRF were significantly higher than cHRF (0.484 and 0.571; $p < 0.001$, $p < 0.01$; Cohen's $d = 1.216, 0.983$). The NRMSE in 1 Hz FT task (0.216) and 2 Hz FT task (0.215) using sHRF were significantly lower than cHRF (0.293 and 0.270; $p < 0.001$, $p < 0.001$; Cohen's $d = 1.494, 1.234$).

The group-averaged optimized HRF parameters are shown in Table III. The parameter c in the 2 Hz FT task (4.385) was significantly larger than the 1 Hz task (2.486, $p = 0.047$), while a_1 decreased in the 2 Hz FT task and the p-value was at a critical value. The parameter c denotes the ratio between the amplitudes of the two gamma functions, with a higher value indicating a reduced undershoot amplitude in the HRF. The parameter a_1 is related to the peak time of the first gamma function, and the smaller a_1 represents the faster rise of the HRF. The changes in parameters c and a_1 indicate that the NVC strength is stronger in the 2 Hz FT task.

Altogether, these qualitative and quantitative results demonstrated the effectiveness of the TRTD method combined with subject-specific optimization of HRF in neurovascular modeling compared to other methods.

IV. DISCUSSION

Exploring NVC using EEG-fNIRS is a feasible solution for various applications due to their good portability, compatibility, and complementarity. Based on our current knowledge, this study stands as the first study to systematically model the EEG-fNIRS NVC and perform a comparison of different EEG features and HRFs with quantitative indicators and cross-validation. To achieve this objective, EEG-fNIRS signals were recorded concurrently during a canonical motor task in neuroimaging experiments, i.e., FT tasks with two speeds. A novel framework was proposed to deal with high-order EEG data and high variability of hemodynamics.

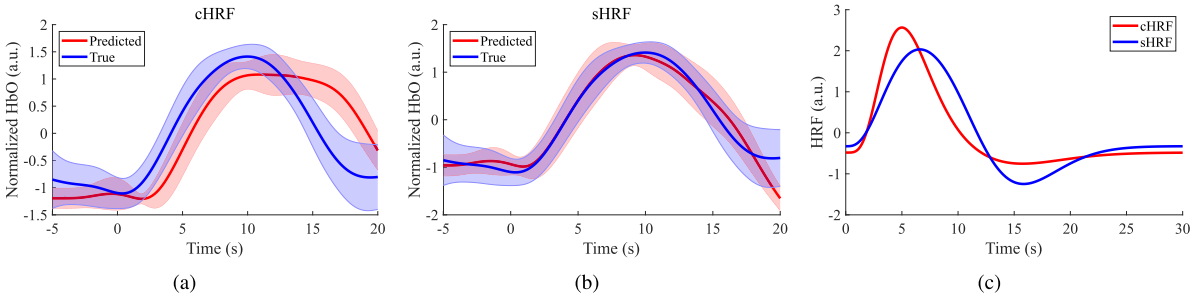

Fig. 9. The comparison of the true HbO signal and the predicted signal fitted by convolving the temporal components of EEG and (a) cHRF and (b) sHRF of a typical participant. The shaded portion of the curve represents the range of standard deviation. (c) the comparison of the cHRF and sHRF.

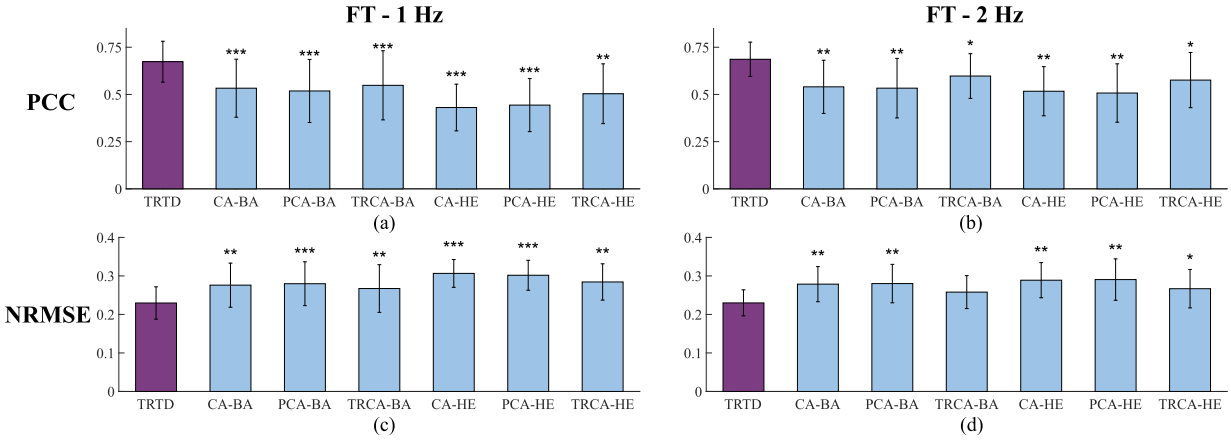

Fig. 10. The PCC and NRMSE between the true HbO signal and the predicted signal fitted by the convolution of the subject-specific HRF and the temporal components decomposed by TRTD and compared methods in two FT tasks. Error bars represent standard deviation. The asterisks '*', '**', and '***' denote $p < 0.05$, $p < 0.01$, and $p < 0.001$, respectively.

TABLE II
THE PCC AND NRMSE BETWEEN THE TRUE HBO SIGNAL AND THE PREDICTED SIGNAL FITTED BY THE TRTD AND COMPARED METHODS

Task	Metrics	Our TRTD method	CA-BA	PCA-BA	TRCA-BA	CA-HE	PCA-HE	TRCA-HE
FT - 1 Hz	PCC	**0.674±0.108**	0.533±0.154	0.518±0.167	0.548±0.183	0.431±0.124	0.444±0.141	0.504±0.158
	p-value		0.001***	0.000***	0.001***	0.000***	0.000***	0.006**
	Effect size		1.086	1.157	1.030	1.571	1.247	0.809
	NRMSE	**0.230±0.042**	0.276±0.057	0.280±0.057	0.267±0.062	0.307±0.036	0.302±0.039	0.284±0.047
	p-value		0.002**	0.000***	0.001**	0.000***	0.000***	0.007**
	Effect size		0.930	1.109	0.984	1.416	1.203	0.787
FT - 2 Hz	PCC	**0.686±0.091**	0.540±0.141	0.533±0.158	0.597±0.118	0.517±0.130	0.507±0.154	0.576±0.146
	p-value		0.007**	0.008**	0.032*	0.002**	0.003**	0.027*
	Effect size		0.782	0.764	0.593	0.936	0.897	0.611
	NRMSE	**0.230±0.034**	0.279±0.046	0.280±0.050	0.258±0.043	0.289±0.046	0.291±0.054	0.267±0.050
	p-value		0.006**	0.007**	0.052	0.002**	0.003**	0.026*
	Effect size		0.799	0.786	0.527	0.954	0.899	0.616

The asterisks '*', '**', and '***' indicate $p < 0.05$, $p < 0.01$, and $p < 0.001$, respectively.

TABLE III
THE GROUP-AVERAGED OPTIMIZED HRF PARAMETERS

	a_1	a_2	b_1	b_2	c
FT - 1 Hz	6.150	15.958	1.492	0.875	2.476
FT - 2 Hz	5.156	17.292	1.364	0.938	4.385
p-value	0.059	0.211	0.254	0.241	0.047*

* indicates significant differences ($p < 0.05$).

Accurate characterization of electrophysiological activity from the EEG signal in relation to task and functional hemodynamic data is the prerequisite for EEG-fNIRS NVC analysis. However, most existing studies used the power fluctuations in distinct frequency bands averaged across predefined ROI as model input, which overlooked the underlying correlation between both intra- and inter-dimensions of high-order EEG data. To this end, we proposed a data-driven analysis framework, TRTD, to decompose the EEG data and extract the task-related temporal components. The group-averaged temporal-spectral-spatial components showed good interpretability. Specifically, the temporal components were closely modulated with the experimental paradigm, which was considered as an indicator of the effectiveness of EEG decomposition [21]. The spectral components indicated that the frequency bands with high weights are mainly distributed

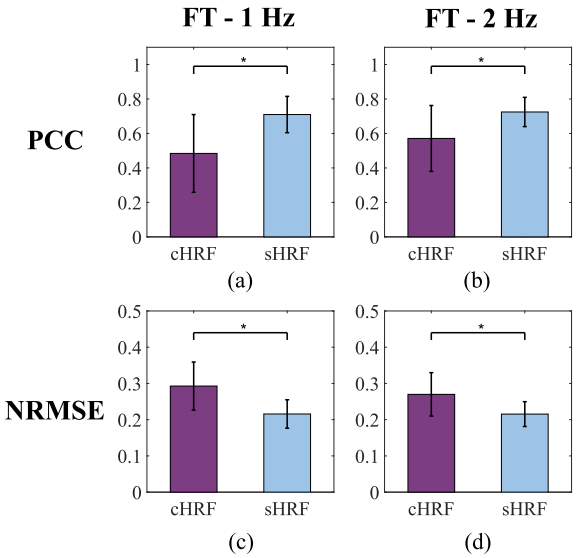

Fig. 11. The PCC and NRMSE between the true HbO signal and the predicted signal fitted by the convolution of the temporal components decomposed by TRTD with the cHRF and sHRF in two FT tasks. Error bars represent standard deviation, and the asterisk '*' denotes $p < 0.05$.

in the alpha, beta, and gamma bands, which were widely proven to be related to motor functions in previous studies [12], [38]. For spatial components, the C3 electrode located at the left M1 had the highest weight. It was reasonable since the activation of M1 in the contralateral brain region has been proven to be a landmark feature during performing FT tasks [39]. The findings demonstrated that TRTD successfully detects the neural activity within the 3D EEG tensor without prior knowledge and effectively addresses the connections among temporal, spectral, and spatial dimensions. In addition, the PCC and NRMSE of TRTD in fitting the fNIRS signals showed significant improvement over the compared methods. Altogether, we concluded that TRTD promises a powerful method for the analysis of the EEG data and has the capacity to offer novel perspectives on the associations between EEG activity and brain hemodynamics.

Having the capacity to precisely quantify the HRF that links the underlying neural activity to the evoked hemodynamic signal is crucial both for exploring the NVC mechanisms and improving the performance of HRF-based analysis for fNIRS signals. In addition, the inter-subject variability in HRF also reinforces the need for its accurate estimation. However, HRF estimation using unimodal fNIRS signal is challenging because of the absence of crucial information regarding the underlying neuronal dynamics. To achieve this objective, employing concurrent EEG-fNIRS recording is a prospective strategy since EEG offers a more direct measurement of neural activations. In this study, we optimized the subject-specific HRF by fitting the convolution of the HRF with the task-related temporal components decomposed by TRTD to the real fNIRS signals. A canonical double gamma function model was used to parameterize the HRF. Constraints were applied to both independent variables and shape parameters to ensure meaningful HRFs. The improvement of the fitting performance including PCC and NRMSE demonstrated the effectiveness of the HRF optimization. In addition, the optimized parameters were demonstrated to have physiological significance and the ability to distinguish the tasks with two speeds. The changes in the parameters c and a_1 indicated that the HbO signal is more activated and the NVC strength was stronger in the 2 Hz task. This is consistent with the GLM analysis result, which indicates the highest activation level of the 2 Hz FT task (0.910) was higher than 1 Hz (0.836). Previous studies also indicated that the faster motor tempo leads to higher fNIRS activation [40]. These physiological parameters were promising for the assessment of the NVC function in patients with neurological disorders such as stroke.

This study has certain limitations. To ensure the signal quality, we only recruited male subjects, which ignores the potential gender differences. Several female subjects were excluded in the preliminary experiment because the fNIRS signal quality was unstable due to the length and density of their hair. As a preliminary attempt, we chose the double gamma function to parameterize the HRF, while its simple structure and intrinsic properties could not completely cover the high variability of neuroimaging signals, thus limiting the performance of the fitting. Future studies will include more HRF models for in-depth validation, such as the Balloon model, which can capture the dynamic changes in blood flow, volume, and oxygenation levels [41]. In addition, this paper analyzed the EEG-fNIRS NVC from the time domain perspective, i.e., the coupling between the amplitude changes of bimodal signals. The coupling of global features including brain networks will be further studied in our future work. Due to the lack of the ground-truth NVC, we used leave-one-out cross validation and designed two task conditions to examine the effectiveness and reproducibility of the proposed framework. Future work will attempt to test the framework in more paradigms. For example, exploring NVC in the occipital lobe during visual stimulation is a viable approach.

V. Conclusion

This paper proposed a new analysis framework to model the subject-specific neurovascular coupling from bimodal EEG-fNIRS measurements. Task-related temporal components were decomposed from the EEG tensor and then fitted to the active fNIRS signal by subject-specific HRF optimization. This method was proven to improve the reproducibility of extracted EEG components and their correlation with both hemodynamic signals and experimental paradigms. Meanwhile, the optimized HRF showed better fitting performance compared to the canonical HRF. Together, the proposed method provides a feasible way to explore the EEG-fNIRS neurovascular coupling.

References

[1] M. Nourhashemi, M. Mahmoudzadeh, S. Goudjil, G. Kongolo, and F. Wallois, "Neurovascular coupling in the developing neonatal brain at rest," *Human Brain Mapping*, vol. 41, no. 2, pp. 503–519, Feb. 2020.

[2] P. S. Hosford and A. V. Gourine, "What is the key mediator of the neurovascular coupling response?" *Neurosci. Biobehavioral Rev.*, vol. 96, pp. 174–181, Jan. 2019.

[3] Y. Gao, H. Liu, F. Fang, and Y. Zhang, "Classification of working memory loads via assessing broken detailed balance of EEG-FNIRS neurovascular coupling measures," *IEEE Trans. Biomed. Eng.*, vol. 70, no. 3, pp. 877–887, Mar. 2023.

[4] F. Almairac, D. Fontaine, T. Demarcy, H. Delingette, S. Beuil, and C. Raffaelli, "Motor cortex neurovascular coupling: Inputs from ultra–high-frequency ultrasound imaging in humans," *J. Neurosurgery*, vol. 131, no. 5, pp. 1632–1638, Nov. 2019.

[5] J. Lin, J. Lu, Z. Shu, N. Yu, and J. Han, "An EEG-fNIRS neurovascular coupling analysis method to investigate cognitive-motor interference," *Comput. Biol. Med.*, vol. 160, Jun. 2023, Art. no. 106968.

[6] C. Iadecola, "The neurovascular unit coming of age: A journey through neurovascular coupling in health and disease," *Neuron*, vol. 96, no. 1, pp. 17–42, Sep. 2017.

[7] W. M. Zhu, A. Neuhaus, D. J. Beard, B. A. Sutherland, and G. C. DeLuca, "Neurovascular coupling mechanisms in health and neurovascular uncoupling in Alzheimer's disease," *Brain*, vol. 145, no. 7, pp. 2276–2292, Jul. 2022.

[8] E. Maggioni et al., "Investigation of the electrophysiological correlates of negative BOLD response during intermittent photic stimulation: An EEG-fMRI study," *Human Brain Mapping*, vol. 37, no. 6, pp. 2247–2262, Jun. 2016.

[9] T. Murta, M. Leite, D. W. Carmichael, P. Figueiredo, and L. Lemieux, "Electrophysiological correlates of the BOLD signal for EEG-informed fMRI," *Human Brain Mapping*, vol. 36, no. 1, pp. 391–414, Jan. 2015.

[10] M. G. Philiastides, T. Tu, and P. Sajda, "Inferring macroscale brain dynamics via fusion of simultaneous EEG-fMRI," *Annu. Rev. Neurosci.*, vol. 44, no. 1, pp. 315–334, Jul. 2021.

[11] H. Laufs et al., "EEG-correlated fMRI of human alpha activity," *NeuroImage*, vol. 19, no. 4, pp. 1463–1476, Aug. 2003.

[12] H. Yuan, T. Liu, R. Szarkowski, C. Rios, J. Ashe, and B. He, "Negative covariation between task-related responses in alpha/beta-band activity and BOLD in human sensorimotor cortex: An EEG and fMRI study of motor imagery and movements," *NeuroImage*, vol. 49, no. 3, pp. 2596–2606, Feb. 2010.

[13] M. Ferrari and V. Quaresima, "A brief review on the history of human functional near-infrared spectroscopy (fNIRS) development and fields of application," *NeuroImage*, vol. 63, no. 2, pp. 921–935, Nov. 2012.

[14] R. Li, C. Zhao, C. Wang, J. Wang, and Y. Zhang, "Enhancing fNIRS analysis using EEG rhythmic signatures: An EEG-informed fNIRS analysis study," *IEEE Trans. Biomed. Eng.*, vol. 67, no. 10, pp. 2789–2797, Oct. 2020.

[15] C. Zhao et al., "The neurovascular couplings between electrophysiological and hemodynamic activities in anticipatory selective attention," *Cerebral Cortex*, vol. 32, no. 22, pp. 4953–4968, Nov. 2022.

[16] D. Mann-Krzisnik and G. D. Mitsis, "Extracting electrophysiological correlates of functional magnetic resonance imaging data using the canonical polyadic decomposition," *Human Brain Mapping*, vol. 43, no. 13, pp. 4045–4073, Sep. 2022.

[17] A.-K. Seghouane and D. Ferrari, "Robust hemodynamic response function estimation from fNIRS signals," *IEEE Trans. Signal Process.*, vol. 67, no. 7, pp. 1838–1848, Apr. 2019.

[18] H. Kang, "Sample size determination and power analysis using the G*Power software," *J. Educ. Eval. Health Professions*, vol. 18, p. 17, Jul. 2021.

[19] M. J. Wessel et al., "Noninvasive theta-burst stimulation of the human striatum enhances striatal activity and motor skill learning," *Nature Neurosci.*, vol. 26, no. 11, pp. 2005–2016, Nov. 2023.

[20] J. Cohen, *Statistical Power Analysis for the Behavioral Sciences*. New York, NY, USA: Academic Press, 2013.

[21] R. Marecek et al., "What can be found in scalp EEG spectrum beyond common frequency bands. EEG-fMRI study," *J. Neural Eng.*, vol. 13, no. 4, Aug. 2016, Art. no. 046026.

[22] M. Lamoš, R. Mareč ek, T. Slavíč ek, M. Mikl, I. Rektor, and J. Jan, "Spatial–temporal–spectral EEG patterns of BOLD functional network connectivity dynamics," *J. Neural Eng.*, vol. 15, no. 3, Jun. 2018, Art. no. 036025.

[23] A. Delorme and S. Makeig, "EEGLAB: An open source toolbox for analysis of single-trial EEG dynamics including independent component analysis," *J. Neurosci. Methods*, vol. 134, no. 1, pp. 9–21, Mar. 2004.

[24] A. Vergult et al., "Improving the interpretation of ictal scalp EEG: BSS-CCA algorithm for muscle artifact removal," *Epilepsia*, vol. 48, no. 5, pp. 950–958, May 2007.

[25] T. J. Huppert, S. G. Diamond, M. A. Franceschini, and D. A. Boas, "HomER: A review of time-series analysis methods for near-infrared spectroscopy of the brain," *Appl. Opt.*, vol. 48, no. 10, p. D280, 2009.

[26] B. Molavi and G. A. Dumont, "Wavelet-based motion artifact removal for functional near-infrared spectroscopy," *Physiol. Meas.*, vol. 33, no. 2, pp. 259–270, Feb. 2012.

[27] S. Jahani, S. K. Setarehdan, D. A. Boas, and M. A. Yücel, "Motion artifact detection and correction in functional near-infrared spectroscopy: A new hybrid method based on spline interpolation method and Savitzky–Golay filtering," *Neurophotonics*, vol. 5, no. 1, 2018, Art. no. 015003.

[28] A. von Lühmann, A. Ortega-Martinez, D. A. Boas, and M. A. Yücel, "Using the general linear model to improve performance in fNIRS single trial analysis and classification: A perspective," *Frontiers Human Neurosci.*, vol. 14, p. 30, Feb. 2020.

[29] F. Cong, Q.-H. Lin, L.-D. Kuang, X.-F. Gong, P. Astikainen, and T. Ristaniemi, "Tensor decomposition of EEG signals: A brief review," *J. Neurosci. Methods*, vol. 248, pp. 59–69, Jun. 2015.

[30] A. Cichocki et al., "Tensor decompositions for signal processing applications: From two-way to multiway component analysis," *IEEE Signal Process. Mag.*, vol. 32, no. 2, pp. 145–163, Mar. 2015.

[31] X. Wang, W. Liu, P. Toiviainen, T. Ristaniemi, and F. Cong, "Group analysis of ongoing EEG data based on fast double-coupled nonnegative tensor decomposition," *J. Neurosci. Methods*, vol. 330, Jan. 2020, Art. no. 108502.

[32] W. Liu, X. Wang, J. Xu, Y. Chang, T. Hämäläinen, and F. Cong, "Identifying oscillatory hyperconnectivity and hypoconnectivity networks in major depression using coupled tensor decomposition," *IEEE Trans. Neural Syst. Rehabil. Eng.*, vol. 29, pp. 1895–1904, 2021.

[33] N. Vervliet, O. Debals, L. Sorber, M. Van Barel, and L. De Lathauwer. (Mar. 2016). *Tensorlab | A Matlab Package for Tensor Computations*. [Online]. Available: https://www.tensorlab.net

[34] H. Tanaka, T. Katura, and H. Sato, "Task-related component analysis for functional neuroimaging and application to near-infrared spectroscopy data," *NeuroImage*, vol. 64, pp. 308–327, Jan. 2013.

[35] B. Maus, G. J. P. van Breukelen, R. Goebel, and M. P. F. Berger, "Optimal design for nonlinear estimation of the hemodynamic response function," *Human Brain Mapping*, vol. 33, no. 6, pp. 1253–1267, Jun. 2012.

[36] J. Ye, S. Tak, K. Jang, J. Jung, and J. Jang, "NIRS-SPM: Statistical parametric mapping for near-infrared spectroscopy," *NeuroImage*, vol. 44, no. 2, pp. 428–447, Jan. 2009.

[37] M. J. Rosa, J. Kilner, F. Blankenburg, O. Josephs, and W. Penny, "Estimating the transfer function from neuronal activity to BOLD using simultaneous EEG-fMRI," *NeuroImage*, vol. 49, no. 2, pp. 1496–1509, Jan. 2010.

[38] C. Park et al., "EEG gamma band oscillations differentiate the planning of spatially directed movements of the arm versus eye: Multivariate empirical mode decomposition analysis," *IEEE Trans. Neural Syst. Rehabil. Eng.*, vol. 22, no. 5, pp. 1083–1096, Sep. 2014.

[39] X. Liao, D. Yao, D. Wu, and C. Li, "Combining spatial filters for the classification of single-trial EEG in a finger movement task," *IEEE Trans. Biomed. Eng.*, vol. 54, no. 5, pp. 821–831, May 2007.

[40] S. M. R. Guérin, M. A. Vincent, C. I. Karageorghis, and Y. N. Delevoye-Turrell, "Effects of motor tempo on frontal brain activity: An fNIRS study," *NeuroImage*, vol. 230, Apr. 2021, Art. no. 117597.

[41] R. B. Buxton, E. C. Wong, and L. R. Frank, "Dynamics of blood flow and oxygenation changes during brain activation: The balloon model," *Magn. Reson. Med.*, vol. 39, no. 6, pp. 855–864, Jun. 1998.